QUANTIFYING SPATIAL-TEMPORAL PATTERN OF URBAN HEAT ISLAND IN BEIJING: AN IMPROVED ASSESSMENT USING LAND SURFACE TEMPERTURE TIME SERIES OBSERVATIONS FROM LANDSAT, MODIS AND CHINESE NEW SATELLITE GAOFEN-1

Kai Liu[1], Hongbo Su[2], Xueke Li[3] and Weimin Wang[4]
[1]Institute of Geographic Sciences and Natural Resources, Chinese Academy of Sciences, Beijing 100101, China
Email: liukai_cas@yahoo.com
[2] Florida Atlantic University, Boca Raton, FL 33431 USA
Email: suh@fau.edu
[3] University of Connecticut, Storrs, Mansfield, CT 06269, USA
Email: xueke.li@uconn.edu
[4]Shenzhen Environmental Monitoring Center, Shenzhen 518049, China
Email: towmwang@163.com

KEY WORDS: Surface urban heat island (SUHI), STARFM, GF-1, Landscape analysis

ABSTRACT: The purpose of this study is to comprehensively quantify the spatial-temporal patterns of surface urban heat island (SUHI) by investigating the relationship between Land surface temperature (LST) and the land-cover types and associated landscape components in the case of Beijing, China. The Spatial and Temporal Adaptive Fusion Model (STARFM) developed by Gao et al. was employed to create the high spatial resolution LST time series, using LST data from the MODIS/Terra and LANDSAT 8 over the period from May to November in 2013. This paper also investigated the application of the Chinese new high spatial resolution satellite GaoFen-1 in urban thermal environments studies which were insufficiently studied previously. The impacts of four Landscape Metrics (LSMs) on urban LST were investigated on the basis of two scenes of GaoFen images acquired in 2013 summer (June 19 and August 10). Results showed that SUHI effect was prevalent in Beijing from May to October. The intensity of SUHI magnitude was found accentuated mainly in the summer months (July and August), indicating the trend of surface UHI effect is inconsistent with that of canopy-layer UHI effect. No obvious linear relationships were observed between mean subplot LST and impervious surfaces LSMs. However, four impervious surfaces LSMs were correlated well with the temporal dynamics of LST. We also found the configurational patterns of green space could put substantial influences as strong as corresponding compositional patterns and the lower vegetation coverage in downtown could better account for the urban LST.

1. INTRODUCTION

Urban microclimate alteration is often closely linked with urban heat island (UHI), which is defined as the phenomenon of higher temperatures occurring in urban areas than in the surrounding rural areas. This phenomenon is widely observed in various cities regardless of their sizes and locations, although with different degree (Oke, 1973). The UHI effect can be evaluated in several ways. In recent years, with the rapid development of earth observation systems, satellite-based imaging technology has been widely applied to study urban climate change (Voogt and Oke, 2003; Yang et al. 2013). In the early stage, NOAA AVHRR and EOS MODIS were used to derive land surface temperature to study urban heat islands (Roth et al. 1989; Tran et al. 2006), yet their spatial resolutions are not fine enough to reveal the detailed spatial pattern of the urban heat variations. More recently, numerous studies on the basis of Landsat TM/ETM, ASTER and HJ-1B data (Cai et al. 2011; Wu et al. 2014), have recently been conducted and achieved good results.

It has been proved by (Roth et al. 1989; Voogt and Oke, 2003) that the most suitable spatial resolution for urban thermal studies is approximately less than 100 m since coarser resolution may result in the loss of details for urban structures. On the other hand, (Liu et al. 2006; Ren et al. 2007) highlighted that there is obvious temporal variability in the SUHI especially during the summer seasons, yet it remains difficult to identify and quantify the variability due to the limited data availability. According to the above two recent findings, fine spatial-temporal resolution of remotely sensed LST data is required in the application of urban thermal environments. Currently, no existing earth observation system could provide remote sensing observations fulfilling the above requirement. It is necessary to develop new and efficient methods that can utilize the observations from multiple satellite sensors to produce a dataset of LST with high spatial-temporal resolution. Gao, et al. developed a Spatial and Temporal Adaptive Reflectance Fusion Model (STARFM), the purpose of which is to retrieve a time series of high spatial resolution images through integrating the low-temporal high spatial resolution imagery and high-temporal low spatial resolution imagery. This model can be applied to simulate a series of surface parameters (e.g. reflectance, albedo, NDVI and temperature). Many applications of the STARFM model in crop yield estimation (Wang et al. 2014; Wenwen et al. 2014), forest classifications (Jia et al. 2014; Walker et al. 2012b) and evapotranspiration research (Cammalleri et al. 2014) have

been conducted, however, much less attention was paid on evaluating the possibility and suitability of applying this method to generate a time series of high spatial resolution LST imagery for monitoring and analyzing complex urban thermal environments.

Composition and configuration are the two essential landscape ecology components for various land cover features especially for impervious surfaces and urban green spaces (Connors et al. 2012; Li et al. 2011). These two landscape ecology components have significantly influenced the establishment and distribution of urban island effects, and thus many studies attempted to investigate the connections between them and LST. Traditional landscape ecology analyses generally tend to focus on static LST scene representing a single state of surface thermal environments observable. Notably, urban landscapes often experience complex surface energy cycle and high variability of meteorological conditions, and thus calling for reliable time series LST data to assess their responses to urban thermal environments for an extended period of time. Despite the popular applications of landscape analysis in various disciplines, surface UHI studies that employed these to examine the connections between landscape components and urban LST, can lead to some intractable problems. One of the important issues is the restricted data availability. Although coarse and medium resolution data (e.g. Landsat and HJ-1) are readily available and widely applied (Wu et al. 2014), coarse pixels contain a combination of different land covers and create problems of mixed pixels over heterogeneous urban areas. Therefore, improving the spatial and temporal resolution of the LST observations from satellites is helpful for urban land cover mapping as well as other landscape related studies.

In this study, we used the latest Version 5 of LST data product from the Terra/MODIS and LANDSAT 8 during the period from May to November in 2013 to assess the spatial and temporal characteristics of SUHI over Beijing, China. This study also attempted to thoroughly investigate the impacts of landscape ecology components on LST by incorporating the two Chinese GaoFen images (GF, meaning "high resolution") acquired in the same summer of 2013 (Li et al. 2015a). As a continuing mission of Chinese HJ-1 (Wang et al. 2010), the High Resolution Earth Observation System includes seven High-Definition Earth Observation Satellites and is to be launched between 2013 and 2016 according to the current plan. The first and second of the series satellites named GF-1 and GF-2 were launched on April 26, 2013 and August 19, 2014, respectively. The imagery of satellite GF-1, which has roughly similar spectral characteristics as HJ-1 CCD and Landsat sensors, may offer new possibilities in extracting the finer spatial features of urban land covers. The primary objectives of this study are to: (1) quantify the trends in the LST time series over various land covers and the associated intensity SUHI, on the basis of high spatial and temporal resolution fused remote sensing data, (2) exam the capability of GF-1 data in facilitating urban land cover mapping and LSMs extracting, and (3) further investigate the quantitative relationships between LST and the LSMs under a multi-temporal framework.

1. STUDY AREA AND DATASETS

1.1 Study Area

Beijing (located between 39°28′N and 41°05 N, 115°25′E and 117°30′E), the capital city of China (seen in Figure 1) was selected as the study area for the present work. This city exhibits a high northwestern and low southeastern terrain, mainly surrounded by mountain areas in the west and plains in the east and south. The temperate continental monsoon climate makes Beijing hot and wet in summer, as well as cold and dry in winter. From May to October Beijing undergoes a warm growing episode for vegetation in both urban and suburban regions. In recent decades, Beijing has experienced a significant urban sprawl. Previous studies, such as (Cai et al. 2011; Ding and Shi, 2013), revealed that Beijing has been experiencing a significant UHI effect resulted from rapid urbanization, and in turn may lead to a series of problems such as the extreme climate and the vulnerable public health.

1.2 Datasets

To analyze the urban thermal pattern of Beijing and explore the associated urban heat island magnitude, six high-quality Landsat 8 images in 2013 (May. 12; June. 13; July. 31; September. 01; October. 01 and November. 04) taken at 10:56 A.M (local time) were collected and processed. Landsat 8 images provide eight visible and infrared bands (1–7 and 9) with a spatial resolution of 30 m, and two thermal infrared bands with a spatial resolution of 100 m. A series of daily MODIS LST (MOD11A1) spanning the hot months from May to November were downloaded through the NASA Atmosphere Archive and Distribution System website data portal available at http://ladsweb.nascom.nasa.gov/data/search.html. These MODIS LST products are used as a reference for the time series high spatial-temporal resolution LST fusing and mapping. Before the fusion process and the SUHI analysis, both the Landsat TIRS and MODIS data were resampled to the same spatial resolution (30 m) and registered to the same UTM coordinate projection.

Two GF-1 images used were acquired on June 19 and August 10 in 2013, both of which are at the ideal time to

identify vegetation growing and capture urban thermal conditions. The Chinese GF-1 satellite performs earth-observation sun-synchronously. GF-1 has six CCD sensors, which can capture ground features with three spatial resolutions at nadir, with four bands covering visible and near-infrared wavelength range and one panchromatic band. More specifically, two of the six sensors constitute an observation network producing the spatial resolution of 2m/8m, while the other four CCDs constitutes an observation network with the spatial resolution of 16 m. The web page of China Center for Resources Satellite Data and Application (http://www.cresda.com/n16/index.html) provides more information about the sensors and data acquisition. In this paper, GF-1 data, which consists of four multispectral bands (red, green, blue and near infrared) at an 8 m spatial resolution and one panchromatic band at a 2 m spatial resolution, were selected.

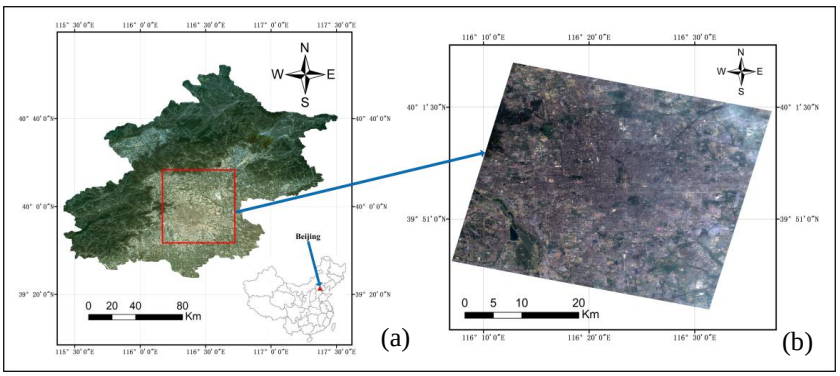

Figure 1 Geographical location of Beijing, China. The region within the red rectangle border is the extent of the analyzed area. The RGB color view in (a) is from LANDSAT acquired on May 12, 2013 and (b) is from GF-1 acquired on August 10, 2013.

2. METHODOLOGY

To quantify the spatial-temporal pattern of LST for Beijing, we first retrieved the LST from the Landsat TIRS band using the single-channel algorithm developed by Jiménez‐Muñoz and Sobrino (2003). Then, high spatial-temporal resolution fused LST images were generated with the STARFM method. Meanwhile, classification and LSMs selection was applied for the GF-1 data. Finally, urban thermal analyses were conducted.

2.1 LST Images Fusion

The spatial and temporal adaptive reflectance fusion model (STARFM) developed by Gao was used to produce Landsat-like LST images based on MODIS daily LST images and LANDSAT LST images. STARFM can simulate new images from the pairs of Landsat and MODIS images acquired on the same day and the MODIS observations from the predicted date. The basic equation of the model is given below:

$$L(X_{w/2}, Y_{w/2}, t_0) = \sum_{i=1}^{W}\sum_{j=1}^{W}\sum_{k=1}^{W} W_{ijk} \times (M(x_i, y_j, t_0) + L(x_i, y_j, t_k) - M(x_i, y_j, t_k)) \quad (1)$$

where L and M refer to the Landsat and MODIS LST separately, (X_i, Y_j) is a given pixel location for a Landsat and MODIS image pair. ($X_{w/2}$, $Y_{w/2}$) is the central pixel of the moving window and ω represents the searching window size. t_0 and t_k are the acquisition date for the simulated date and image pair data, respectively. The weight W_{ijk} is an important parameter that decides the impact of each neighboring pixel on the simulated central pixel. This variable is determined by three components: temporal difference between the predicted data and input MODIS images, LST values difference between Landsat and MODIS images, and the spatial distance between the central pixel and the moving window.

This study implemented the STARFM model to predict LANDSAT-like LST for images dated on 05/20/2013, 05/30/2013, 06/23/2013, 07/02/2013, 07/12/2013, 07/24/2013, 08/10/2013, 08/18/2013, 09/11/2013, 09/21/2013, 10/15/2013, and 10/25/2013. These twelve dates were considered as representatives of the twelve study periods. We performed this algorithm to each of pair images using a moving window size of 1500 ×1500 m and a band uncertainty parameter of 0.005, according to the study of (Hilker et al. 2009; Walker et al. 2012a).

2.2 Retrieval of Land-cover Classify Map and Delineation of Urban Region

Land-cover features were mapped through image classification for Landsat OLI images. This study adopted a non-parametric supervised classification based on statistical learning theory, the support vector machine (SVM) classification approach. Five predominated land-cover types (i.e., forest, crops/grassland, bare soil, impervious surfaces and water bodies) were identified for the six scenes of LANDSAT OLI images acquired in 2013. The pan-sharpened multi-spectral GF-1 data, with a spatial resolution of 2 m, were also used to recognize fine urban land covers as well as extracting LSMs. An object-based classification approach was carried out using the Feature Extraction tool in ENVI 5.0. The four bands blue, green, red and near-infrared were all used for classification. The main land cover features considered in the present study are forest/urban trees, bare soil, water bodies, impervious surfaces, and crops/grassland. Since the SUHII was defined as the LST difference between urban region and its surrounding suburban area, we have to extract the urban region of the Beijing for the UHI magnitude analysis. Following the study outlined in (Zhou et al. 2014), we delineated the urban and suburban area based on the different levels of impervious surfaces density.

2.3 Urban Landscape Metrics Selection

Four most important and commonly used LSMs were computed to investigate the correlation of LST and LSMs during the hot or warm days. The percentage of land cover (PLAND) was selected to measure the composition information. The land configuration metrics include patch density (PD), edge density (ED) and largest patch index (LPI). More detailed calculation equations can be found in (McGarigal et al. 2002). These four LSMs were selected since they can provide mutual complementary and meaningful information in delineating landscape components related to both composition and configuration.

Landscape analysis was carried out using the collected high spatial resolution data, 2 × 2 m GF-1 pan-sharpened classification result. In this study, a subset of 14×14 km sample plot in both images over the downtown of Beijing was carefully chosen to represent the dominant city landscape structures. We further divided the 14×14 km plot into 196 subplots of 1×1 km in size, thereby a statistical analysis could be conducted using each subplot as a processing unit. The LSMs were calculated with the FRAGSTATS software (McGarigal et al. 2002). It should be mentioned that present study only considered two major land covers including impervious surfaces and vegetation cover, since these two cover types hold a very considerable fractional area in most cities.

3. RESULTS

3.1 Implementation of Classification Mapping and LSMs Selection

Figure 2(a) gives an example of the classification map derived from LANDSAT OLI images. All the six images achieved agreeable results with the OA higher than 85% and KC higher than 0.90, indicating the resultant OLI classifications are reliable for further analysis. In addition, to improve the land-cover classification, the classification results were then manually refined with the incorporation of visual interpretations. Figure 2(b) exhibits the urban and suburban areas used for calculating SUHII. The urban and suburban areas were determined using the Landsat OLI image acquired on 07/31/2013. Since there was no significant change of the impervious surfaces density from May to November in 2013, we assume that the urban and suburban boundaries delineated on 07/31/2013 can be used to represent the whole study period in 2013.

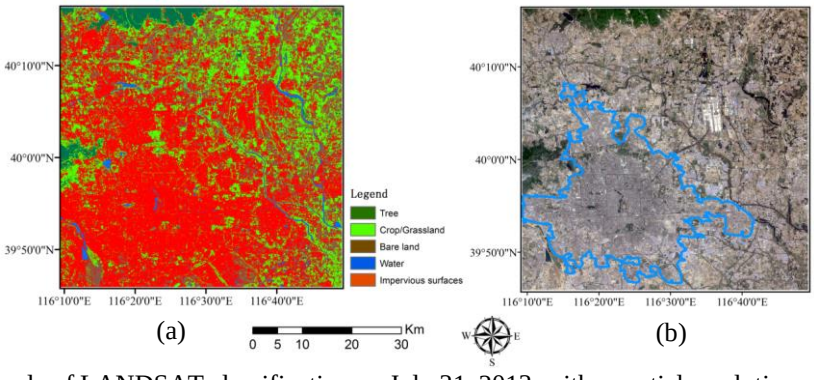

Figure 2 (a) An example of LANDSAT classification on July 31, 2013, with a spatial resolution of 30m×30m. (b) The delineation of urban and suburban areas of Beijing. The blue line stands for the border of urban area, the land within the border was considered as the urban area, and that the region outside of the blue line represents the suburban area.

To accurately classify the urban dominated land covers (seen in Figure 3) from a high resolution satellite data, our

work adopted the object-based classification approach to enhance class contrast and to avoid the salt and pepper phenomena commonly found in classifications of urban scenes. The OA of 94.33% and 95.56% was achieved by combining SVM and OBIA for the two scenes of GF-1 in this study, while the KC was 0.94 and 0.93 respectively. Concerning the urban green types, with the user's and producer's accuracies of 86.8% and 93.6% for the scene of June 19 and 89.3% and 94.2% for the scene of August 10, most of the pixels covered by the actual trees and grassland were found to have been accurately identified. Meanwhile, the vast majority of small and patches of shrubs regions have also been recognized, most of which are difficult to identify due to the adjacent interference from built-up and road network especially for coarser resolution imagery. Despite that there existed a small fractional of spurious impervious surfaces regions which are actually urban greens, most of the built-up and pavements in the scene were correctly identified. Overall, this work demonstrated the potential capability of classification using pan-sharpened images from GF-1 satellite over urban areas.

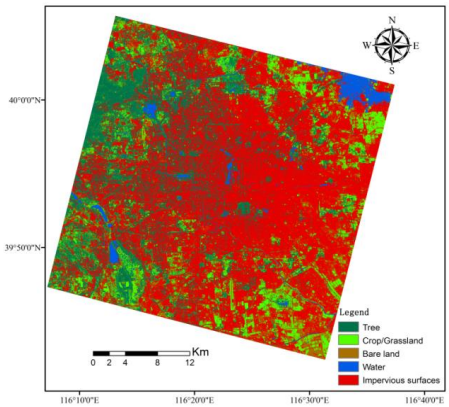

Figure 3 An example of GF-1 classification on August 10, 2013, with a spatial resolution of 2m×2m.

3.2 Implementation of Fused High Spatial Resolution LST

Figure 4 gives Landsat LST images and Figure 5 exhibits the predicted LANDSAT-like LST images using the STARFM method. Results show that all the images exhibited basically the similar spatial pattern except for the date of 11/04/2013. Inspection of the time series of LANDSAT LST reveals that urban center exhibits the higher LST for the warmer days, while the LST tends to decrease from the urban downtown area to the surrounding suburban regions.

To evaluate the performance of the STARFM algorithm in the LST series fusion over Beijing, a number of samples containing 200*200 pixels (approximately 10% of the study area) were randomly selected to compare the predicted LST on 07/31/2013 (summer day) and 10/03/2013 (autumn day) with the reference LST acquired by Landsat TIRS on 07/31/2013 and 10/03/2013. It could be seen from the scatter plots of estimated and reference LST data (seen in Figure 6 (a) and (b)) that most of points were scattered along the 1:1 line for the two images. The determination coefficient R^2 was 0.71 and 0.84 (significant levels < 0.05), and the RMSE was 1.79 K and 1.36 K respectively. Results shown that predicted LANDSAT-like LST data using STARFM may slightly underestimate the LST especially for densely urbanized regions on 07/31/2013 (seen in Figure 6(a)). This may be associated with the date interval of data acquisition, the uncertainties from atmospheric correction, and the residual errors from geometric registration. Overall, the comparison of predicted LANDSAT-like and reference Landsat LST lends support to the application of STARFM in combing the strengths of both MODIS and Landsat LST.

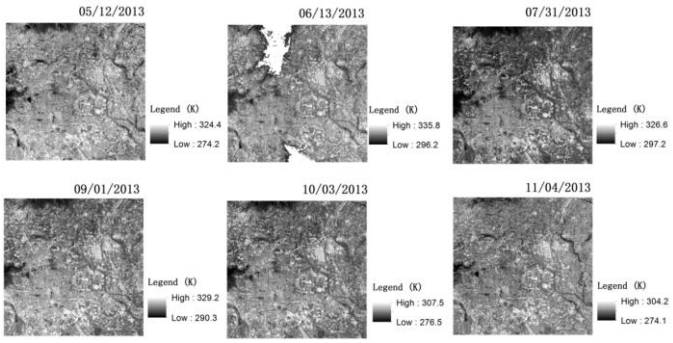

Figure 4 The Landsat LST images used as the base images for the fusion model (White points were identified and masked out due to cloud contamination).

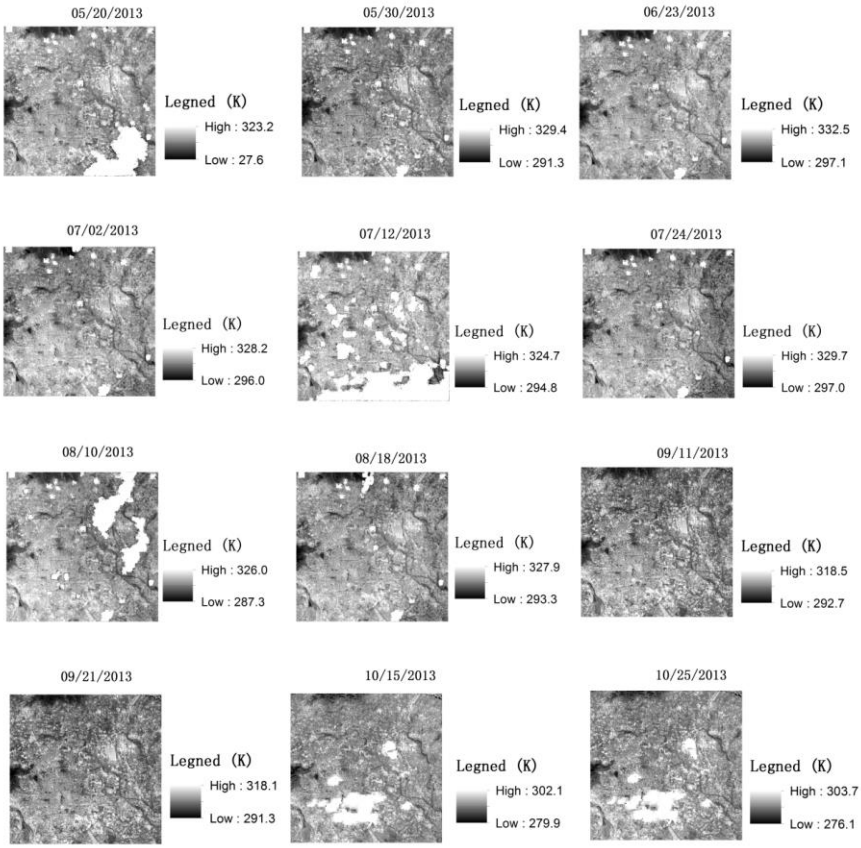

Figure 5 The fused Landsat LST images (White points were identified and masked out due to cloud contamination).

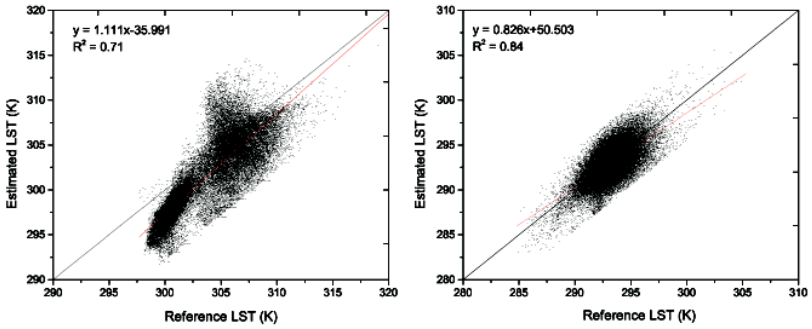

(a) (b)

Figure 6 Scatter plots of fused LST and reference LST on (a) 07/31/2013 and (b) 10/03/ 2013.

Using the LANDSAT LST retrieval and land-cover classification maps obtained from LANDSAT OLI, we investigated the LST of each land-cover type in the urban areas as well as the suburb regions of Beijing. Figure 7(a) reveals that various land-cover types in the whole study areas exhibited obvious discrepancy in LST. For the study period excluding the November, vegetated cover (main suburb forest and urban greens) had relatively lower temperatures, while surface temperatures of impervious surfaces and bare soil were much higher. Water bodies mainly including the rivers, pools and reservoirs occupied the lower values in LST, yet higher than forest in some cases by 0-2 K. Concerning the urban regions only (seen in Figure 7(b)), the highest LST was primarily distributed in the commercial districts and dense residential areas, where the major land-cover type was various impervious surfaces such as building and diverse pavements. The mean LST of the impervious surface areas was higher than that of the urban greens (grassland and urban trees) which are mainly located around the parkland and residential areas.

Temporal variability of LST among various land-cover types existed through the time from May to October. Figure 7 shows the discrepancy in LST appeared to be more significant in summer days (from June to August) than other days (May, from September to November) for the whole study region. More specifically, we found the difference between impervious surfaces and vegetation cover was 4 - 9 K in the hotter months (July and August), while it dropped to less than 4 K during the relatively warmer season (May and October). Regarding the urban regions only, the difference between impervious surfaces and urban greens was 5–8 K in the hotter months (July and August), and decreasing to less than 5 K for other days.

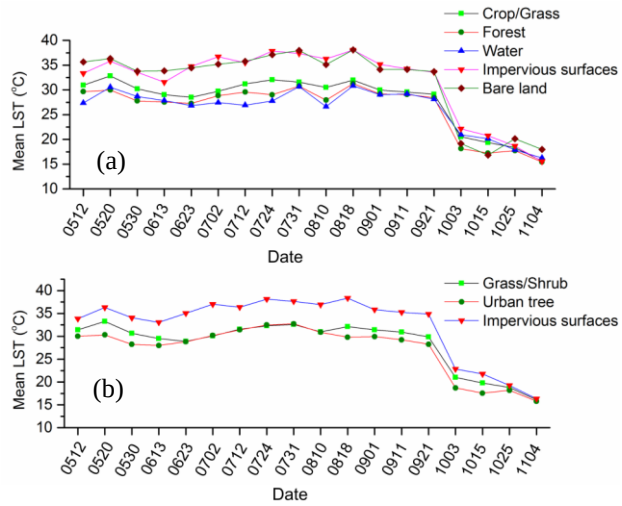

Figure 7 Mean LST for different land surfaces from May to November in (a) the whole study area and (b) the urban region.

This study also investigated the magnitudes of SUHI, which were calculated from both the reference data and predicted LST images. The SUHII, which was computed using the method introduced in section III, varied throughout the study period, showing a mean of 2.3 K. Furthermore, there existed an intermonth low and high variation trend in the SUHII, with a standard deviation of 1.15 K. During the summer days, the SUHII shows higher values, while lower values in the other months. More specifically, the retrieval SUHII was accentuated mainly in the summer months (July and August) with a value of 3–4 K compared to less 3 K during the relatively warmer season (May and October). Also shown in Figure 10 is the SUHII temporal cycle derived from the MODIS daily LST and the MODIS 8-day composition LST. SUHII from three data sources are similar in magnitude trends, yet values of SUHII from Landsat LST are generally higher than the MODIS based SUHII.

3.3 Relationship of LSMs and LST

In order to assess the impact of impervious surfaces compositions and configurations on urban surface temperatures, the Person's correlation coefficient between four LSMs and subplot mean LST were calculated and shown in Figure 8. It shows a rather weak positive relationship trend among the mean subplot LST and PLAND, ED, PD, and LSI with respect to impervious surfaces. These relationships do not seem to be statistically significant enough $R < 0.35$ (in all cases, significant levels < 0.05) to draw more concrete quantitative conclusions. However, a general agreement in the tendency of these relationships regarding to the temporal variability was found, and that the positive correlation was more substantial in the hotter summer compared to other warmer days. For the four LSMs, the highest R was found to be 0.35 (in July 31), 0.22 (in July 31), 0.33 (in July 12), and 0.33 (in July 12) respectively.

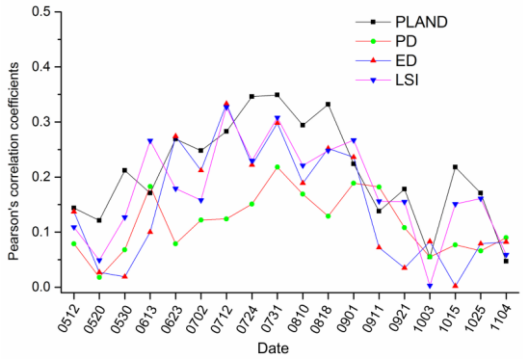

Figure 8 The Person's correlation coefficients between LST and Impervious surfaces LSMs.

On the other hand, to carefully exam the impacts of urban greens on urban LST, we used two scenes of LST image which has the acquisition time closest to each GF-1 images we have, one is the reference TIRS LST and the other is the STARFM predicted LANDSAT-like LST. Scatter plots and determination coefficient R^2 between mean subplot LST and urban greens LSMs were calculated. Figure 9 and Figure 10 show that R^2 among the mean subplot LST and urban greens LSMs basically gives similar values for the two pairs original TIRS LST and predicted LST on two different dates. It is evident that the compositional and spatial configuration of urban green space can impact the LST to some extent. Results shown that mean LST was negatively correlated with the four LSMs of urban greens.

Contrarily to impervious surfaces, these landscape-LST relationships seem to be statistically rather deterministic regarding urban greenspace. PLAND was correlated with mean LST, ranging from 0.39 to 0.57 for R^2. The other three metrics were observed of different R^2, typically with mean value of 0.19, 0.45 and 0.37 for PD, ED and LSI respectively.

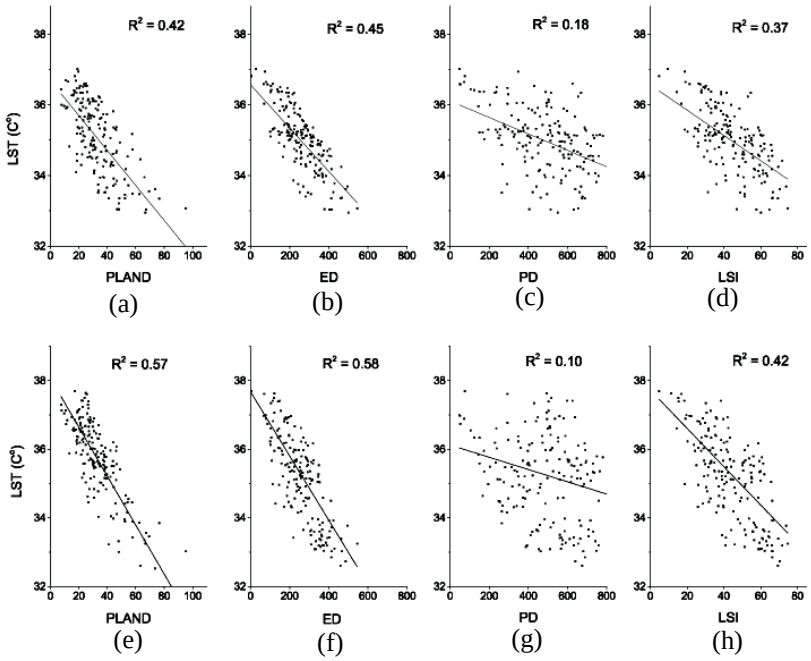

Figure 9 Scatters plots of mean LST and urban greens LSMs on 06/19/2013. (a-d) LANDSAT LST; (e-h) Predicted LANDSAT-Like LST

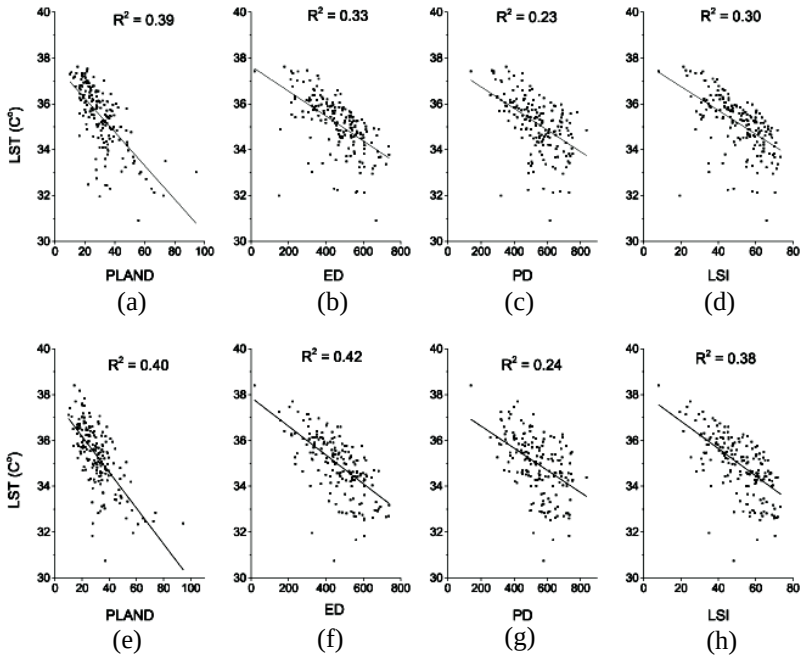

Figure 10 Scatters plots of mean LST and urban greens LSMs on 08/10/2013. (a-d) LANDSAT LST; (e-h) Predicted LANDSAT-Like LST

4. DISCUSSION

Results in almost all the selected image scenes consistently suggested that land-cover types play a role in impacting the distribution of urban thermal pattern through the time from May to October. The apparent temporal variation trends were observed in the daytime SUHI. The SUHI effect was exhibited obviously from June to October, and reached a peak in July and August. Weaker SUHI effects could be found in May and November. In contrast to the prior studies of (Liu et al. 2007; Santamouris 2015), which delineated canopy layer UHI effect with air temperature data from automatic weather stations and reported that the UHI reaches its minimum during the humid summer days,

we found that surface UHI effect is much more significant during the summer. This might be partly ascribed to the surface characteristics and increasing anthropogenic heat emission mainly from urban energy and transportation systems during the hot season in this region. Our finding is supported by previous studies (Li et al. 2014; Sailor and Lu, 2004), which reported that the seasonal variability of urban thermal energy balance was caused mainly by the magnitude of the anthropogenic heat released.

For the urban districts of the Beijing, results showed that urban trees had stronger cooling effects than grassland/shrubs for most of the study period, similar to the results of many UHI studies (Rahman et al. 2011; Shashua-Bar et al. 2009). Interestingly, we noticed the mean LST of urban trees was slightly higher than or the same as that of grassland/shrub in late June and early July by 0.5-1 K. This is probably because that the grassland/shrub could have a higher evapotranspiration rate than patches of trees due to the impacts of continental monsoon climate characterized by rainy summers. Similar results were found in (Peters et al. 2011), which reported that turfgrass contributed more annual evapotranspiration over dense impervious surfaces due to its higher average rates of water use in midsummer than the urban trees in the Minneapolis-Saint Paul metropolitan. According to this, it appears that increasing the area of grass/shrub in urban regions is a good alternative to reduce the UHI effect on condition that to plant urban trees is impractical, although most previous studies reported that tree planting can effectively lower the temperature of built-up surfaces due to the combined oasis and clothesline effects.

Previous urban thermal studies generally using a static LST image reported that percentage coverage of urban impervious surfaces play a significant role in affecting urban LST. This study focused on investigating the impacts of compositional impervious surfaces on the pattern of short-term urban surface temperature on the basis of the series LST images in Beijing. Although these impacts were obvious at a specific time, the relationship within a short term may not be significant enough to draw a definite conclusion. This implies that percentage coverage of urban impervious surfaces may be not an overwhelmingly dominant factor in determining the magnitude of LST in the case of Beijing. Despite that the R^2 of ED, LSI and subplot LST of impervious surfaces was larger than those of their corresponding composition variables at some specific times, the configuration variables' relationship with LST remained as weak as that of their corresponding composition variables. This can be attributed to the fact that the local urban surface thermal pattern is not only affected by the involved impervious surfaces conditions, but also by other factors such as vegetation activity, anthropogenic heat releases and the continental monsoon climate.

For the urban greens LSMs, PLAND has a strong reverse correlation with the subplot LST in summer days for both two image pairs, implying that the composition of urban greens is an essential factor in cooling urban LST. Moreover, we found that the configuration of urban greens features also impacts urban LST. This is consistent with other prior studies (Maimaitiyiming et al. 2014; Wu, 2008), which reported that LST could be changed with the modification of spatial configuration of urban greens. Our study shows the configurationally green space patterns do have relatively substantial influences basically as strong as their compositional green space patterns, such as ED, LSI and PLAND, which could explain 30% - 60% of the spatial variations of urban LST (seen in Figure. 13 and Figure. 14). This may be associated with the fact that higher edge density and shape complexity of urban greens can enhance the mutual interactions between urban greenspaces and buildings, thus facilitating energy exchange involved as well resulting in a lower local LST. In addition, it is worthwhile to note that PD and ED are both correlated variables but exhibit different levels of impacts on urban LST. Results show that ED has more significant effects on LST than PD, with an R^2 approximately larger by 0.2. According to this, we suggest that planting the urban greens in an even distribution rather than a scattered clustering distribution pattern be more effective in cooling the urban surfaces in Beijing.

5. SUMMARY AND CONCLUSIONS

This paper focused on delineating the spatial-temporal variation of thermal patterns in the urban area of Beijing using satellite observations from Landsat, MODIS, and GF-1. The validation showed that STARFM-predicted LST and reference surface temperatures were closely correlated. These results indicate that the predicted LST products derived from STARFM are acceptable to be used in the investigation of the spatial and temporal characteristics of urban thermal environments of Beijing. On the other hand, this paper demonstrates the capability of applying the observations from the newly launched Chinese high spatial resolution satellite GF-1 in urban thermal environments studies as well as landscape ecological analyses which were not sufficiently investigated in previous studies.

REFERENCES

C. Cammalleri, M. C. Anderson, F. Gao, C. R. Hain, and W. P. Kustas, 2014. Mapping daily evapotranspiration at field scales over rainfed and irrigated agricultural areas using remote sensing data fusion. Agricultural and Forest Meteorology, vol. 186, pp. 1-11.

C. Li, J. Zhou, Y. Cao, J. Zhong, Y. Liu, C. Kang, et al., 2014. Interaction between urban microclimate and electric air-conditioning energy consumption during high temperature season. Applied Energy, vol. 117, pp. 149-156.

C. Wenwen, S. Jinling, W. Jindi, and X. Zhiqiang, 2014. High spatial-and temporal-resolution NDVI produced by the assimilation of MODIS and HJ-1 data. Canadian Journal of Remote Sensing, vol. 37, pp. 612-327.

D. Armson, P. Stringer, and A. R. Ennos, 2012. The effect of tree shade and grass on surface and globe temperatures in an urban area. Urban Forestry & Urban Greening, vol. 11, pp. 245-255.

D. J. Sailor and L. Lu, 2004. A top–down methodology for developing diurnal and seasonal anthropogenic heating profiles for urban areas. Atmospheric Environment, vol. 38, pp. 2737-2748.

D. Zhou, S. Zhao, S. Liu, L. Zhang, and C. Zhu, 2014. Surface urban heat island in China's 32 major cities: Spatial patterns and drivers. Remote Sensing of Environment, vol. 152, pp. 51-61.

E. B. Peters, R. V. Hiller, and J. P. McFadden, 2011. Seasonal contributions of vegetation types to suburban evapotranspiration. Journal of Geophysical Research: Biogeosciences (2005–2012), vol. 116.

F. Gao, J. Masek, M. Schwaller, and F. Hall, 2006. On the blending of the Landsat and MODIS surface reflectance: Predicting daily Landsat surface reflectance. Geoscience and Remote Sensing, IEEE Transactions on, vol. 44, pp. 2207-2218.

G. Cai, M. Du, and Y. Xue, 2011. Monitoring of urban heat island effect in Beijing combining ASTER and TM data. International Journal of Remote Sensing, vol. 32, pp. 1213-1232.

H. Wu, L.-P. Ye, W.-Z. Shi, and K. C. Clarke, 2014. Assessing the effects of land use spatial structure on urban heat islands using HJ-1B remote sensing imagery in Wuhan, China. International Journal of Applied Earth Observation and Geoinformation, vol. 32, pp. 67-78.

J. A. Voogt and T. R. Oke, 2003. Thermal remote sensing of urban climates. Remote Sensing of Environment, vol. 86, pp. 370-384.

J. C. Jiménez - Muñoz and J. A. Sobrino, 2003. A generalized single - channel method for retrieving land surface temperature from remote sensing data. Journal of Geophysical Research: Atmospheres (1984–2012), vol. 108.

J. Li, X. Chen, L. Tian, J. Huang, and L. Feng, 2015. Improved capabilities of the Chinese high-resolution remote sensing satellite GF-1 for monitoring suspended particulate matter (SPM) in inland waters: Radiometric and spatial considerations. ISPRS Journal of Photogrammetry and Remote Sensing, vol. 106, pp. 145-156.

J. J. Walker, K. M. de Beurs, R. H. Wynne, and F. Gao, 2012. Evaluation of Landsat and MODIS data fusion products for analysis of dryland forest phenology. Remote Sensing of Environment, vol. 117, pp. 381-393.

J. J. Wu, 2008. Making the case for landscape ecology an effective approach to urban sustainability. Landscape Journal, vol. 27, pp. 41-50.

J. P. Connors, C. S. Galletti, and W. T. L. Chow, 2012. Landscape configuration and urban heat island effects: assessing the relationship between landscape characteristics and land surface temperature in Phoenix, Arizona. Landscape Ecology, vol. 28, pp. 271-283.

K. Gallo, A. McNab, T. Karl, J. Brown, J. Hood, and J. Tarpley, 1993. The use of NOAA AVHRR data for assessment of the urban heat island effect. Journal of Applied Meteorology, vol. 32, pp. 899-908.

K. McGarigal, S. A. Cushman, M. C. Neel, and E. Ene, 2002. FRAGSTATS: spatial pattern analysis program for categorical maps.

K. Jia, S. Liang, L. Zhang, X. Wei, Y. Yao, and X. Xie, 2014. Forest cover classification using Landsat ETM+ data and time series MODIS NDVI data. International Journal of Applied Earth Observation and Geoinformation, vol. 33, pp. 32-38.

L. Wang, Y. Tian, X. Yao, Y. Zhu, and W. Cao, 2014. Predicting grain yield and protein content in wheat by fusing multi-sensor and multi-temporal remote-sensing images. Field Crops Research, vol. 164, pp. 178-188.

L. Shashua-Bar, D. Pearlmutter, and E. Erell, 2009. The cooling efficiency of urban landscape strategies in a hot dry climate. Landscape and Urban Planning, vol. 92, pp. 179-186.

M. Roth, T. Oke, and W. Emery, 1989. Satellite-derived urban heat islands from three coastal cities and the utilization of such data in urban climatology. International Journal of Remote Sensing, vol. 10, pp. 1699-1720.

M. Rahman, J. Smith, P. Stringer, and A. Ennos, 2011. Effect of rooting conditions on the growth and cooling ability of Pyrus calleryana. Urban Forestry & Urban Greening, vol. 10, pp. 185-192.

M. Santamouris, 2015. Analyzing the heat island magnitude and characteristics in one hundred Asian and Australian cities and regions. Science of The Total Environment, vol. 512, pp. 582-598.

P. Coseo and L. Larsen, 2014. How factors of land use/land cover, building configuration, and adjacent heat sources and sinks explain Urban Heat Islands in Chicago. Landscape and Urban Planning, vol. 125, pp. 117-129.

Q. Wang, C. Wu, Q. Li, and J. Li, 2010. Chinese HJ-1A/B satellites and data characteristics. Science China Earth Sciences, vol. 53, pp. 51-57.

S. Peng, S. Piao, P. Ciais, P. Friedlingstein, C. Ottle, F. M. Breon, et al., 2012. Surface urban heat island across 419 global big cities. Environ Sci Technol, vol. 46, pp. 696-703.

T. Hilker, M. A. Wulder, N. C. Coops, N. Seitz, J. C. White, F. Gao, et al., 2009. Generation of dense time series synthetic Landsat data through data blending with MODIS using a spatial and temporal adaptive reflectance fusion model. Remote Sensing of Environment, vol. 113, pp. 1988-1999.

Y. Sun, X. Zhang, F. W. Zwiers, L. Song, H. Wan, T. Hu, et al., 2014. Rapid increase in the risk of extreme summer heat in Eastern China. Nature Climate Change, vol. 4, pp. 1082-1085.